Dual-Inverter-Integrated Three-Phase EV Charger Based on Split-Phase Machine

Caniggia Viana, *Student Member, IEEE*, Mehanathan Pathmanathan, *Senior Member, IEEE*, and Peter W. Lehn, *Senior Member, IEEE*

***Abstract*— Significant effort has been dedicated to developing integrated onboard charging circuits for electric vehicles, aiming to improve cost, range anxiety, and charging convenience. The dual-inverter drivetrain topology has attracted particular attention as a platform for developing such solutions, being previously leveraged for the implementation of dc and single-phase ac onboard charging. This work proposes an integrated three-phase onboard charger based on the dual-inverter drivetrain. The proposed converter is implemented with minimal change to the dual inverter and no additional power electronics by introducing a split-phase electric machine. A mathematical model is developed, decomposing the system into four decoupled subsystems, individually responsible for charging, driving, grid common-mode current, and zero-sequence current generation, respectively. In light of this model, a novel space-vector pulsewidth modulation technique is introduced to ensure charging current control while generating no flux-producing, nor zero-sequence currents, and having superior common-mode performance. Simulation-based and experimental verification is conducted on a 7.2-kW scaled-down prototype to prove the charging concept, as well as the common-mode current elimination.**

***Index Terms*—Electric vehicle (EV) drivetrain, integrated charger, modeling and control, onboard charger, transformerless.**

I. Introduction

ELECTRIC vehicles (EVs) have recently gained significant momentum. The market share and the variety of commercially available models have grown over the last decade. While transportation electrification has moved forward, cost, range anxiety, and charging inconvenience have consistently been identified as factors slowing EV adoption by the consumer market [1]–[3].

One of the significant strategies to improve such factors is the development of integrated charging topologies, an approach reviewed in [4]–[6]. This strategy leverages preexisting parts of the vehicle, such as the drivetrain, to implement the onboard charger. Several integrated charging solutions have been proposed for charging. Some approaches are as follows:

Manuscript received 22 February 2022; revised 17 May 2022; accepted 26 June 2022. Date of publication 30 June 2022; date of current version 6 September 2022. This work was supported in part by Havelaar, the University of Toronto Havelaar Electric Vehicle Research Center through sub-project: multi-port converters under Grant 501508, and in part by NSERC CRD, high-efficiency electric vehicle drivetrains with integrated fast charging and dual storage media under Grant 503979. Recommended for publication by Associate Editor D. Zhang. *(Corresponding author: Caniggia Viana.)*

The authors are with the Department of Electrical and Computing Engineering, University of Toronto, Toronto, ON M5S1A4, Canada (e-mail: caniggiadiniz@gmail.com; meha.pathmanathan@utoronto.ca; lehn@ecf.utoronto.ca).

Color versions of one or more figures in this article are available at https://doi.org/10.1109/TPEL.2022.3187568.

Digital Object Identifier 10.1109/TPEL.2022.3187568

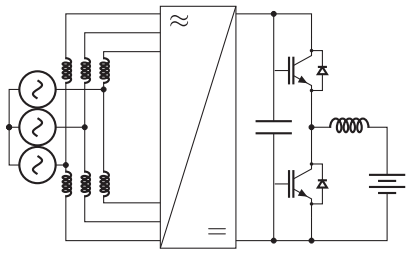

Fig. 1. Integrated three-phase charger with split-phase open winding motor architecture and six-leg inverter drivetrain [16].

1) Deploying multiphase machines for driving and using the multiple neutral points of these machines to interface the grid [7], [8], such that the machine leakage inductance filters the switching content produced by the inverter during charging operation. For these solutions, the drivetrain inverter is the only power electronics required.
2) Using a front-end current source converter, and conducting current through the zero-sequence of the machine, leveraging its leakage inductance [9]–[11].
3) Using a front-end converter, and conducting current through the positive sequence of the machine [12]. While this solution utilizes the machine's full magnetizing inductance, it requires a front-end converter and produces significant torque at the grid frequency.
4) Using a dual-inverter drivetrain, fed by a dual battery pack, with the machine leakage inductance used for filtering purposes and common-mode voltage between both batteries being used to oppose a single-phase ac or dc grid [13]–[15].

One of the approaches used to implement three-phase integrated chargers relies on the use of split-phase open wound motors. These motors have each one of the stator phases split into two windings, hereinafter termed half-windings (HWs). The connection point between two HWs is used to interface a three-phase grid, as shown in Fig. 1. With an appropriate modulation and control scheme, the current can divide equally between the top and bottom HWs of each phase, with the magnetic field generated, by a given HW, through the rotor canceling its complementary HW. As a result, the charger leverages the machine leakage inductance without producing any torque while using the inverter to produce grid-opposing voltage. Systems based on this idea are explored in [16]–[20].

A similar approach has been used with asymmetrical six-phase machines. In this strategy, contactors are used to

reconfigure the motor when in charging mode, enabling grid connection. During driving, all phases of the machine are connected, forming a neutral point. Solutions exploring this strategy are discussed in [21]–[23], including control strategies to minimize torque production. Also using contactors, some works have proposed integrated battery chargers using three-phase single inverters and split-phase machines [24], [25]. While these solutions can be beneficial in some scenarios, given the high current ratings required for driving, contactors may become significantly costly and, in some applications, impractical.

While the approaches previously discussed stand to significantly improve EV mass and production cost, they all fail to address the issue of grid common-mode (CM) leakage currents, and therefore run the risk of being impractical. Defined as the sum of the currents flowing from all connection points to the grid, CM currents can represent a safety hazard. To prevent such hazard, some standards pose strict limits on CM currents and require the inclusion of a ground fault current interrupter, designed to trip and open the circuit when the CM current exceeds 20 MIU, i.e., 20 mA_{peak} at the output of a prescribed low-pass filter [26], [27]. The issue is particularly pronounced for the solution introduced in [9], which has been commercialized and has been reported to suffer with CM-induced nuisance tripping.

Interest in transformerless and integrated chargers has been documented. Yet, while CM currents have been extensively addressed in photovoltaic generation [28]–[30], there are few solutions addressing CM voltage production for integrated chargers [31]–[33]. Zhang *et al.* [34] list, as possible solutions, 1) disconnection of dc-link capacitors, which is not feasible in commercial vehicles, 2) excessive ac CM filtering, which may be expensive, 3) alternative modulation schemes, and 4) active CM filters, which might be infeasible due to the increased complexity. A prominent solution suggests grounding the vehicle chassis through a high impedance [35]. While this solution does reduce grid leakage currents, it jeopardizes the guaranty of zero touch potential at the chassis. A safer solution to enable the benefits of transformerless integrated chargers can therefore be greatly beneficial.

This article introduces a novel topology, featuring the dual-inverter drivetrain, fed by a dual battery pack, driving a split-phase machine. This drivetrain is selected as a base for the integrated charging topology due to its previously explored competitive driving features: 1) It operates well over a wide range of speeds [36]; 2) it has improved current switching harmonic profile [37], [38]; 3) it shows resiliency under some faults [39], [40]; and 4) it can be used to control power flow between the two dc-links' energy sources [41], [42].

The main contributions of this work are as follows:

1) A novel topology, leveraging the dual inverter to implement an integrated three-phase charger. The dual inverter may be driven by either a single battery pack or a dual battery pack. The dual battery pack operation first explored in this work presents the advantage over single-battery solutions, of having no path for zero-sequence circulating currents in the machine. Thus, regardless of the modulation choice, the detrimental impacts of zero-sequence currents are not experienced during any operation.

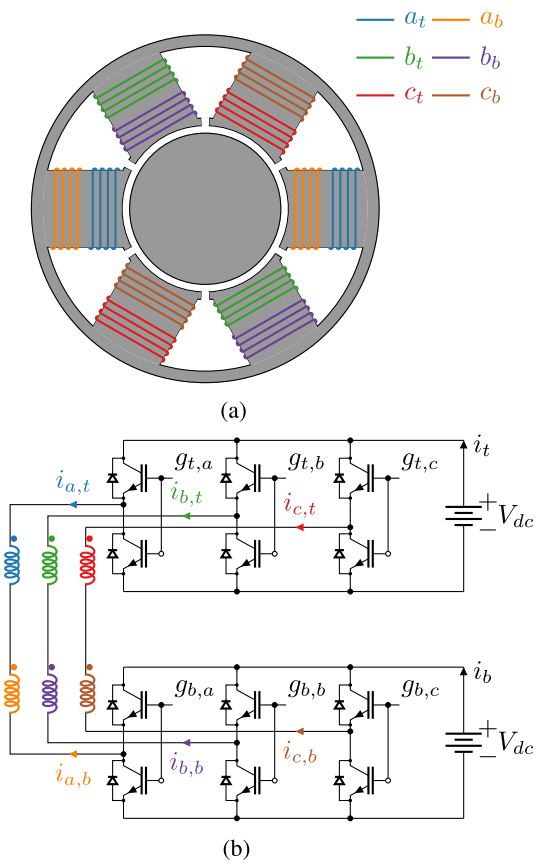

Fig. 2. Proposed drivetrain with a dual inverter controlling a split-phase, open winding machine. (a) Schematic representation of split-phase open winding machine. (b) Proposed dual-inverter architecture.

2) A mathematical model, applicable not only to the proposed dual-battery topology but also to single-battery split-phase machine drivetrains, detailing the six available degrees of freedom and how they relate to driving, charging, zero-sequence current, and CM current production.
3) A novel modulation that, using the insights afforded by the aforementioned model, enables standard-compliant CM charging operation, rendering practical not only the presently proposed charger, but also the charger explored in the body of work composed of [16]–[20], while also ensuring zero torque production during charging operation.

II. Proposed Topology

The proposed topology consists of a drivetrain formed by a split-phase open winding machine driven by a dual-inverter architecture. A representation of the machine's stator is provided in Fig. 2(a), where, without loss of generality, a two-pole stator and round rotor are depicted. The dual inverter and its connection to the machine are shown in Fig. 2(b).

A variety of rotor types are suitable for implementing this system, without significant difference in charging functionality, including slip ring, squirrel cage, permanent magnet, and wound synchronous rotor. Therefore, only the rotor magnetic core is represented in Fig. 2(a). The drivetrain can be operated in driving mode using a classic control strategy appropriate to the rotor

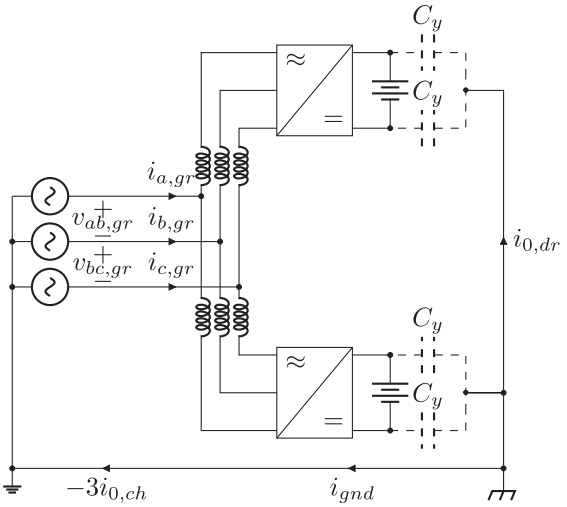

Fig. 3. Three-phase charging configuration of the system.

type. Since the driving operation is extensively discussed in the literature, the topic is not addressed in this work, other than demonstrating that charging operation does not result in torque production via analysis, simulation, and experimental results.

To operate the system in charging mode, a three-phase grid can be connected to the split-phase point of each phase of the machine, as shown in Fig. 3. During charging operation, the vehicle's chassis is assumed to be connected to ground via a protective earth conductor to ensure zero potential at the accessible chassis, as required by the standard. The current flowing through the protective earth conductor, i_{gnd}, by standard, is required to be monitored by a residual current monitoring device, which interrupts the charging process if the value exceeds a specified threshold. In that context, the y-capacitances, present between the battery and chassis, become relevant, as these components complete the path through which i_{gnd} may flow. The y-capacitances can be included, by design, as a discrete component, or arise due to parasitic effects in the system. Given the presence of y-capacitances and protective earth conductor in the system, as shown in Fig. 3, it is necessary to devise and consider the CM model of the system, taking measures to ensure low CM currents during the charging process in order to avoid nuisance tripping of protective systems.

A. Model and Operating Principle

A generalized Clarke transformation can be defined to decompose the system into six components. The voltage resulting from the transformation is described in (1a), whereas the current is described in (1b).

$$\begin{bmatrix} v_{\alpha,dr} \\ v_{\beta,dr} \\ v_{0,dr} \\ v_{\alpha,ch} \\ v_{\beta,ch} \\ v_{0,ch} \end{bmatrix} = V_{\text{dc}} \begin{bmatrix} C & -C \\ \frac{1}{2}C & \frac{1}{2}C \end{bmatrix} \begin{bmatrix} g_{a,t} \\ g_{b,t} \\ g_{c,t} \\ g_{a,b} \\ g_{b,b} \\ g_{c,b} \end{bmatrix} - \begin{bmatrix} 0 \\ 0 \\ 0 \\ 0 \\ 0 \\ \frac{V_{dc}}{2} \end{bmatrix} \tag{1a}$$

$$\begin{bmatrix} i_{\alpha,dr} \\ i_{\beta,dr} \\ i_{0,dr} \\ i_{\alpha,ch} \\ i_{\beta,ch} \\ i_{0,ch} \end{bmatrix} = \begin{bmatrix} \frac{1}{2}C & -\frac{1}{2}C \\ C & C \end{bmatrix} \begin{bmatrix} i_{a,t} \\ i_{b,t} \\ i_{c,t} \\ i_{a,b} \\ i_{b,b} \\ i_{c,b} \end{bmatrix}. \tag{1b}$$

In (1),

1) the gating pulses are defined to be 1, when the associated transistor is ON and 0 otherwise;
2) C is the 3×3 Clarke transformation matrix, defined as
$$C = \frac{2}{3} \begin{bmatrix} 1 & -\frac{1}{2} & -\frac{1}{2} \\ 0 & \frac{\sqrt{3}}{2} & -\frac{\sqrt{3}}{2} \\ \frac{1}{2} & \frac{1}{2} & \frac{1}{2} \end{bmatrix} \tag{2}$$
3) the charging voltage space-vector is defined as
$$\vec{v}_{ch} = v_{\alpha,ch} + j v_{\beta,ch} \tag{3}$$
and represents the voltage used to control the charging current;
4) the driving voltage space-vector is defined as
$$\vec{v}_{dr} = v_{\alpha,dr} + j v_{\beta,dr} \tag{4}$$
and represents the voltage used to generate magnetic flux through the rotor and control torque production;
5) the quantity $v_{0,dr}$ represents the zero-sequence voltage applied to the motor terminals by the dual inverter;
6) the quantity $v_{0,ch}$ represents the CM voltage applied in the direction of producing CM leakage current through the ac grid;
7) $\vec{i}_{gr} = -\vec{i}_{ch} = -(i_{\alpha,ch} + j i_{\beta,ch})$ is space-vector current flowing through the three-phase grid connection;
8) $\vec{i}_{dr} = i_{\alpha,dr} + j i_{\beta,dr}$ is the driving current, which produces rotating flux through the rotor;
9) $i_{0,dr}$ is the zero-sequence current flowing through the machine; and
10) $i_{\text{gnd}} = -3i_{0,ch}$ is CM leakage current flowing through the grid.

Combined, these two transformations result in the definition of four submodels, respectively, associated with each one of the subsystems' effects: Driving, charging, zero-sequence, and CM current. As shown by the model, the four subsystems are mathematically and conceptually decoupled from one another.

The system can, then, be understood as four subsystems, which combined account for the six degrees of freedom of the total system.

1) The charging subsystem, comprising $\vec{i}_{ch}$, $\vec{v}_{ch}$, and, when present, $\vec{v}_{gr}$, describes the current exchange via the split-phase connection of the machine and accounts for two degrees of freedom.
2) The driving subsystem, comprising $\vec{i}_{dr}$, $\vec{v}_{dr}$, and, when moving, $\vec{v}_{\text{bemf}}$, describes the two degrees of freedom responsible for torque production.
3) The zero-sequence subsystem, comprising $i_{0,dr}$ and $v_{0,dr}$, describes the generation of zero-sequence current through the machine stator windings.

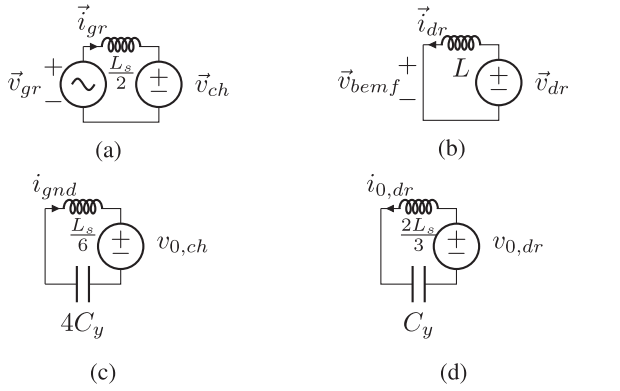

Fig. 4. Decoupled representation of the four subsystems resulting from the proposed topology during charging operation. L_s represents the machine's per-phase leakage inductance and L represents the positive sequence inductance. $\vec{v}_{\text{bemf}}$ is the back electromotive force produced by the machine. C_y is the y-capacitance coupling each battery to the vehicle's chassis. (a) Charging model. (b) Driving model. (c) Grid CM leakage model. (d) Machine zero-sequence model.

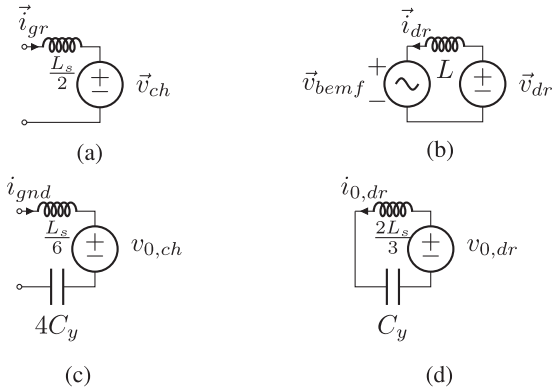

Fig. 5. Decoupled representation of the four subsystems resulting from the proposed topology during driving operation. (a) Charging model. (b) Driving model. (c) Grid CM leakage model. (d) Machine zero-sequence model.

4) The CM subsystem, comprising $i_{0,ch}$ and $v_{0,ch}$, describes the generation of CM current through the grid.

Note that these subsystems describe the degrees of freedom associated with each operation. As a mathematical description, the subsystems exist even when they are idle. For instance, the charging system exists even when the vehicle is not charging.

For illustration purposes, the four subsystems are shown in this section. A nonsalient permanent magnet synchronous machine (PMSM) is chosen for this representation, since the machine model is the simplest. However, the proposed approach is valid for different rotor types. In fact, to demonstrate this flexibility, the experiments are conducted on an IM.

During charging operation, the three-phase grid is connected to the system, providing the voltage space-vector, $\vec{v}_{gr}$, from which the system charges by transferring power via the model represented in Fig. 4(a). In this condition, the grid connection and the protective earth connection provide a path for CM leakage current through the y-capacitances, as represented in Fig. 4(c).

During charging operation, for safety reasons, the machine must remain stationary. This is achieved by applying $\langle \vec{v}_{dr} \rangle = 0$. For induction machines, this approach ensures the stator is not excited, therefore not producing any torque. For PMSMs, zero-driving voltage implements an active short and acts like an virtual strong brake [43], [44], thereby locking the rotor in place.

The system is assumed to be disconnected from the grid and protective earth conductor during driving operation. As a result, the subsystems represented in Fig. 5(a) and (c) feature an open-circuit, signifying the lack of a current carrying path. The model relevant for driving operation is represented in Fig. 5(b) and includes a nonzero $\vec{v}_{\text{bemf}}$, produced by the machine as a result of nonzero speed. No significant changes are observed in the zero-sequence model.

A control system for driving operation can be devised using the submodel depicted in Fig. 5(b). The submodels represented in Fig. 5(a) and (c) do not need be considered in the control design, as current flow through the associated degrees of freedom is not possible. The model represented Fig. 5(d) may, in some circumstances, be neglected, as the typically small values of C_y result in a high impedance, which renders the magnitude of $i_{0,dr}$ insignificant for the system.

During charging operation, the system must control the charging voltage $\vec{v}_{ch}$. In order to avoid torque production, it is desired that the average driving voltage $\vec{v}_{dr}$ over a switching cycle is 0. Finally, the system is designed not to require galvanic isolation. Therefore, the instantaneous voltage $v_{0,ch}$ must be 0 at all times, in order to mitigate CM current production and meet the strict CM standard requirements. It is important to note that, in contrast with the model represented in Figs. 4(d) and 5(d), the model in Fig. 4(c) must be carefully considered, as even CM leakage currents in the mA range may cause nuisance tripping. In Section III-B, a modulator is proposed to ensure the conditions stated in this paragraph are met, allowing the system to charge while not producing torque, zero-sequence current through the machine, or CM currents through the grid.

III. Control System

By virtue of the decoupled nature of the four subsystems, it is possible to devise a control architecture that tracks a desired charging current by applying a suitable value of $\vec{v}_{ch}$ to the system, while not generating any current through the other subsystems. In this section, the control architecture which determines the reference voltage $\vec{v}^*_{ch}$ is briefly discussed. A novel modulator is then introduced, which, in light of the four subsystems introduced in Section II-A, synthesizes

$$\langle \vec{v}_{ch} \rangle = \vec{v}^*_{ch} \tag{5a}$$

outputting the reference voltage produced by the control system, while ensuring

$$\langle \vec{v}_{dr} \rangle = 0 \tag{5b}$$

thereby preventing torque production

$$\langle v_{0,dr} \rangle = 0 \tag{5c}$$

and, most importantly,

$$v_{0,ch}(t) = 0 \ \forall t \tag{5d}$$

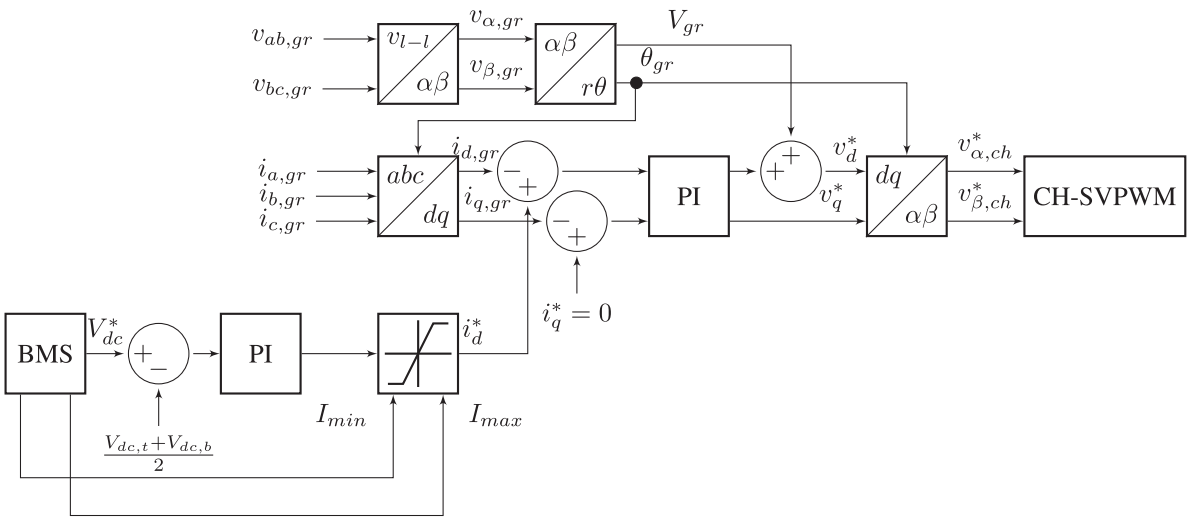

Fig. 6. Control architecture used during charging operation of the proposed integrated drivetrain charger.

eliminating CM voltage generated by the system. In (5), $\langle x \rangle$ represents the average, over a switching cycle, of the quantity x, whereas (5d) refers to the instantaneous value of $v_{0,ch}$.

The control system architecture used in the simulations and experiments performed in this article is shown in Fig. 6 and implements a version of the conventional constant voltage–constant current (CC-CV) charging algorithm. In the control system depicted in Fig. 6, the line-to-line voltages at the grid connection are measured, and a Clarke transformation is used to express the voltages in the stationary reference frame (SRF). The result is fed into a rectangular-to-polar transformation to determine the magnitude of the grid voltage, V_{gr}, and the associated angle, θ_{gr}. The line currents are measured and transformed into a rotating reference frame (RRF) aligned with θ_{gr}. The CV controller determines the required current coming from the grid in order to bring the average battery voltage to the reference value V_{dc}^*, defined by a battery management system (BMS). The result is saturated to a maximum current to produce the current reference i_d^*, which the CC controller enforces. The BMS defines the saturation limits, considering the battery and grid current capabilities. Unity power factor is enforced by defining $i_q^* = 0$. The output of the current controller is added to a feedforward voltage based on the grid voltage, and the result is rotated back to the SRF. Finally, this voltage is sent to the proposed charging space-vector modulator (CH-SVPWM), described in Section III-B.

A. Available Switching States

In order to ensure minimal leakage current, $\frac{d}{dt} v_{0,ch} = 0$ must be respected at all times. Applying $v_{0,ch} = 0$ achieves this objective while allowing for maximum available number of switching states. It is, therefore, convenient to list all of the possible switching states at which $v_{0,ch} = 0$. Table I lists all such states, and accounts for 20 of the total 64 possible switching states. In the table, $\vec{v}_{dr}$, $v_{0,dr}$, and $\vec{v}_{ch}$ are also shown.

The space-vector diagrams resulting from Table I are shown in Fig. 7. Fig. 7(a), on the left, shows the attainable nonzero

TABLE I
SWITCHING STATES PRODUCING 0 CM VOLTAGE

State	$g_{a,t}g_{b,t}g_{c,t}g_{a,b}g_{b,b}g_{c,b}$	$\vec{v}_{dr}$	$v_{0,dr}$	$\vec{v}_{ch}$	$v_{0,ch}$
0	1 0 1 0 0 1	$\frac{2V_{dc}}{3}\angle 0°$	$\frac{V_{dc}}{3}$	$\frac{V_{dc}}{\sqrt{3}}\angle -90°$	0
1	0 0 1 1 0 1	$\frac{2V_{dc}}{3}\angle 180°$	$-\frac{V_{dc}}{3}$	$\frac{V_{dc}}{\sqrt{3}}\angle -90°$	0
2	1 0 1 1 0 0	$\frac{2V_{dc}}{3}\angle -120°$	$\frac{V_{dc}}{3}$	$\frac{V_{dc}}{\sqrt{3}}\angle -30°$	0
3	1 0 0 1 0 1	$\frac{2V_{dc}}{3}\angle 60°$	$-\frac{V_{dc}}{3}$	$\frac{V_{dc}}{\sqrt{3}}\angle -30°$	0
4	1 1 0 1 0 0	$\frac{2V_{dc}}{3}\angle 120°$	$\frac{V_{dc}}{3}$	$\frac{V_{dc}}{\sqrt{3}}\angle 30°$	0
5	1 0 0 1 1 0	$\frac{2V_{dc}}{3}\angle -60°$	$-\frac{V_{dc}}{3}$	$\frac{V_{dc}}{\sqrt{3}}\angle 30°$	0
6	1 1 0 0 1 0	$\frac{2V_{dc}}{3}\angle 0°$	$\frac{V_{dc}}{3}$	$\frac{V_{dc}}{\sqrt{3}}\angle 90°$	0
7	0 1 0 1 1 0	$\frac{2V_{dc}}{3}\angle 180°$	$-\frac{V_{dc}}{3}$	$\frac{V_{dc}}{\sqrt{3}}\angle 90°$	0
8	0 1 1 0 1 0	$\frac{2V_{dc}}{3}\angle -120°$	$\frac{V_{dc}}{3}$	$\frac{V_{dc}}{\sqrt{3}}\angle 150°$	0
9	0 1 0 0 1 1	$\frac{2V_{dc}}{3}\angle 60°$	$-\frac{V_{dc}}{3}$	$\frac{V_{dc}}{\sqrt{3}}\angle 150°$	0
10	0 1 1 0 0 1	$\frac{2V_{dc}}{3}\angle 120°$	$\frac{V_{dc}}{3}$	$\frac{V_{dc}}{\sqrt{3}}\angle -150°$	0
11	0 0 1 0 1 1	$\frac{2V_{dc}}{3}\angle -60°$	$-\frac{V_{dc}}{3}$	$\frac{V_{dc}}{\sqrt{3}}\angle -150°$	0
12	1 0 0 0 1 1	$\frac{4V_{dc}}{3}\angle 0°$	$-\frac{V_{dc}}{3}$	0	0
13	1 1 0 0 0 1	$\frac{4V_{dc}}{3}\angle 60°$	$\frac{V_{dc}}{3}$	0	0
14	0 1 0 1 0 1	$\frac{4V_{dc}}{3}\angle 120°$	$-\frac{V_{dc}}{3}$	0	0
15	0 1 1 1 0 0	$\frac{4V_{dc}}{3}\angle 180°$	$\frac{V_{dc}}{3}$	0	0
16	0 0 1 1 1 0	$\frac{4V_{dc}}{3}\angle -120°$	$-\frac{V_{dc}}{3}$	0	0
17	1 0 1 0 1 0	$\frac{4V_{dc}}{3}\angle 60°$	$\frac{V_{dc}}{3}$	0	0
18	1 1 1 0 0 0	0	V_{batt}	0	0
19	0 0 0 1 1 1	0	$-V_{batt}$	0	0

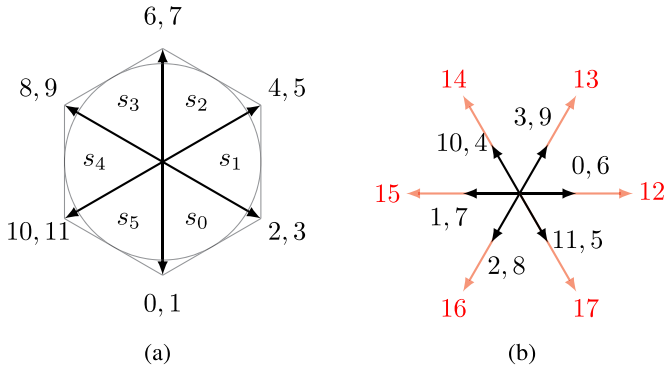

Fig. 7. Available voltage space-vector with zero CM voltage. Zero vectors not labeled. (a) Available charging voltage space-vector, $\vec{v}_{ch}$. (b) Available driving voltage space-vector, $\vec{v}_{dr}$.

charging voltage space-vectors, whereas Fig. 7(b), on the right, shows the nonzero driving voltages space-vectors, as defined in Section II-A.

B. Proposed Modulation

The modulator is devised constraining the system to the switching states presented in Table I, inherently ensuring (5d) and, as a result, minimal CM leakage current generated by the charger. The generalized description of the modulator, which can be used for implementation, is provided in Appendix A. The discussion presented in this section assumes, without loss of generality, a reference voltage in sector s_0 [as defined in Fig. 7(a)], for simplicity. Under this simplifying assumption, the sequence of switching states used by the system, over one switching period, is

$$18 \rightarrow 0 \rightarrow 3 \rightarrow 19 \rightarrow 1 \rightarrow 2 \rightarrow 18.$$

The synthesized charging voltage, averaged over a switching period, is given by

$$\left\langle \begin{bmatrix} v_{\alpha,ch} \\ v_{\beta,ch} \end{bmatrix} \right\rangle = \frac{V_{\mathrm{dc}} f_{\mathrm{sw}}}{\sqrt{3}} \begin{bmatrix} 0 & \frac{\sqrt{3}}{2} \\ -1 & -\frac{1}{2} \end{bmatrix} \begin{bmatrix} t_0 + t_1 \\ t_2 + t_3 \end{bmatrix} \tag{6}$$

where t_x is the time spent at switching state x. This method can ensure the condition stated in (5a) by determining the dwell times as

$$\begin{bmatrix} t_0 \\ t_2 \end{bmatrix} = \begin{bmatrix} t_1 \\ t_3 \end{bmatrix} = \frac{\sqrt{3}}{2V_{\mathrm{dc}} f_{\mathrm{sw}}} \begin{bmatrix} 0 & \frac{\sqrt{3}}{2} \\ -1 & -\frac{1}{2} \end{bmatrix}^{-1} \begin{bmatrix} v^*_{\alpha,ch} \\ v^*_{\beta,ch} \end{bmatrix}. \tag{7}$$

Another implication of (7) is that (5b) is also met. This is a result of the three factors that

1) switching states 0 and 1 produce diametrically opposed instantaneous driving voltage;
2) $t_0 = t_1$, canceling the contribution of each switching state;
3) the same happens for switching states 2 and 3.

Finally, this approach can also meet condition (5c), by setting $t_{18} = t_{19}$, equaling dividing the remaining of the switching period between these two states. The zero-sequence voltage is canceled because each one of the following pairs of switching states cancels the contribution toward $\langle v_{0,dr} \rangle$: states 0 and 1, states 2 and 3, and states 18 and 19. Note that this approach does not use the switching states 12–17 since these states' zero-charging vector can be achieved by simply using states 18 and 19.

IV. Simulations

The system shown in Fig. 2 is simulated using the parameters listed in Table II. L_s refers to the leakage inductance of the machine across each HW. Similarly, R_s refers to the resistance through one HW. Note that the impedance seen by the charging operation is half of that of a HW, given the parallel connection. Similarly, the maximum charging current is twice the rated phase current.

The parameters used in the simulation are based on those used for experimental verification, presented later in this work. The experimental setup, in turn, is a scaled-down model of the proposed system, given the limitations imposed by the available induction machine. To operate with a 400 V_{rms} line voltage grid, for instance, while maintaining the $\vec{v}_{ch}$ inside of the feasible region, described in Fig. 7(a), the minimum dc-link battery, at the lowest state of charge (SoC), should be

$$V_{\mathrm{dc}} \leq 400 \frac{2\sqrt{2}}{\sqrt{3}} + \sigma \approx 653\ V + \sigma \tag{8}$$

where σ is an appropriate safety margin.

At time $t = 0$, the reference charging current is stepped up from 0 to 20 A. The converter starts switching at the same time. Grid line currents and phase voltages are shown in Fig. 8. The currents are sinusoidal and in phase with the grid voltage.

The system is assumed to be operating in CC mode. Therefore, the current reference is immediately stepped up. The control response is shown in Fig. 9, where the currents have been transformed to the RRF for ease of interpretation. The d-axis current reference is the one to increase, as this axis is connected to active power exchange with the grid. On the other hand, the

TABLE II
Parameters Used in Simulations and Experiments

Parameter	Description	Value
Battery Voltages	V_{dc}	400 V
Switching Frequency	f_{sw}	10 kH
Grid Voltage	V_{gr}	208 V_{rms}
Rated Machine Data		
Leakage Inductance	L_s	6 mH
Line Voltage	V_m	230 V_{rms}
Line Current	I_m	10 A_{rms}
Phase Resistance	R_s	0.5 Ω
Nominal Power	P_m	15 hp
Nominal Torque	T_{qm}	30 Nm

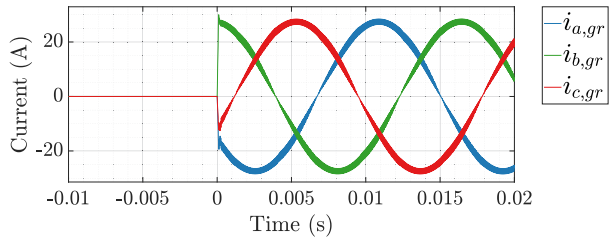

(a)

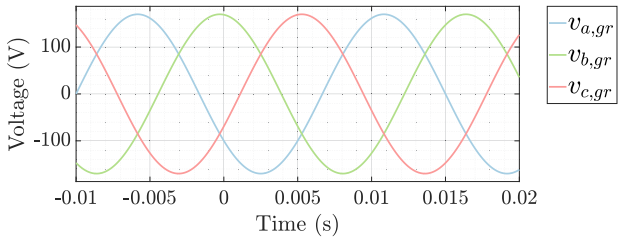

(b)

Fig. 8. Grid phase quantities under transient step in charging current reference. (a) Grid current. (b) Grid voltage.

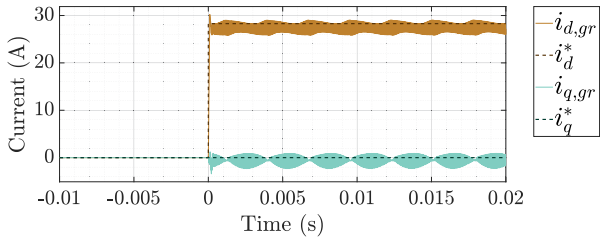

Fig. 9. Direct-axis representation of the grid current and its reference value from simulation.

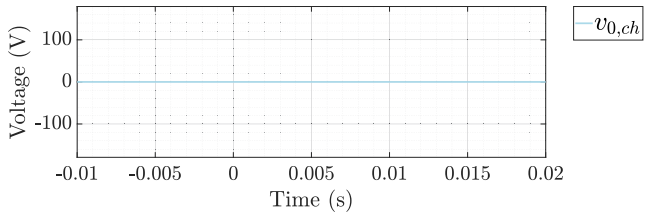

Fig. 10. CM voltage space-vector generated by the dual inverter during charging operation.

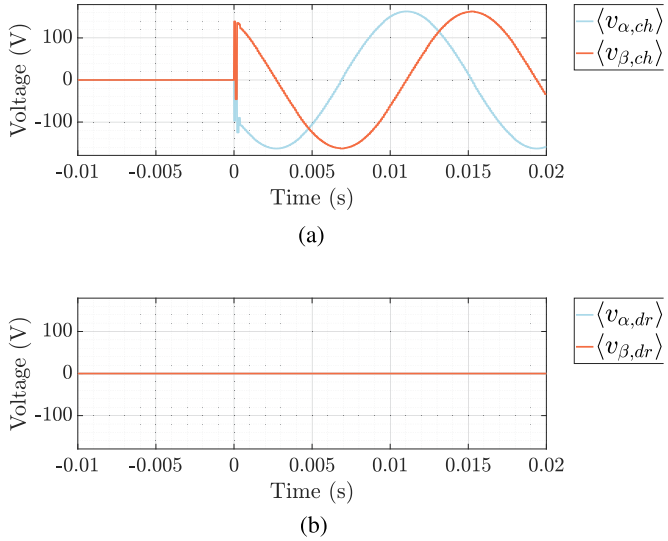

Fig. 11. Voltage space-vectors decomposed as defined in (1), averaged over a switching cycle. (a) Charging voltage space-vector in SRF. (b) Driving voltage space-vector in SRF.

q-axis reference is kept at 0, as this axis is related with reactive power and unity power factor is desired.

The CM voltage produced by the inverter is measured. The results are shown in Fig. 10. It can be observed that the proposed modulator ensures zero instantaneous CM voltage at all times in simulation.

The voltage produced by the inverter in simulation is averaged over a switching period and transformed according to (1), from which the space-vector charging and driving voltages are shown in Fig. 11. The charging voltage space-vector is shown in Fig. 11(a) and both the α and β components are sinusoidal. The averaged driving voltage is shown in Fig. 11(b), confirming it is zero, as desired, by how the modulation is implemented. Combined, these two results highlight how the modulator can produce controllable charging voltage while producing zero flux-generating voltage.

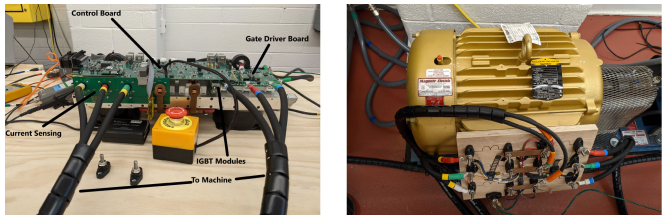

(a) (b)

Fig. 12. Setup used for experimental verification. (a) Power electronics. (b) Induction motor.

V. Experimental Verification

The system discussed above is implemented for experimental verification. In this analysis, the parameters are identical to those used in simulation. The experimental setup is shown in Fig. 12. The motor used in this setup is a three-phase Baldor EM2394 T, modified to have open winding and each phase split into two HWs, as shown in Fig. 2. The machine has the same resistance as stated in Table II. A digital torque transducer, model DR-2412-P, from LORENZ MESSTECHNIK GmbH, is included to demonstrate zero torque production. A specialized Rogolski coil is used to measure the CM current flowing from the grid.

The experiments presented in this section are as follows:

1) grid-to-vehicle operation with a conventional sinusoidal PWM modulation, providing a benchmark for the production of CM currents;
2) grid-to-vehicle operation, showcasing zero torque production and near-zero CM currents;
3) vehicle-to-grid operation, showcasing zero torque production and near-zero CM currents; and
4) constant current–constant voltage charging operation, demonstrating operation in a realistic charging regiment.

In the first experiment, the circuit shown in Fig. 2 is used to charge from the three-phase grid, at 20 A_{rms} and unity power factor. In this test, a conventional PWM modulation, explicitly defined in (9), is used to serve as a baseline for CM production. This test uses the control architecture shown in Fig. 6. The grid line currents and phase voltage are shown in Fig. 13(a). The CM current, shown in Fig. 13(b), is measure to be 2.0 A_{rms} and, as demonstrated later in this article, well above the limits prescribed by standard regulation. Moreover, the high-sensitivity current sensor used to measure the CM current has a maximum instantaneous readable current amplitude of 2.5 A, and a clear clipping effect is observed, in Fig. 13(b), around 3 A, suggesting the actual RMS CM current is well above the measured value.

$$\begin{bmatrix} v_{a,t}^* \\ v_{b,t}^* \\ v_{c,t}^* \end{bmatrix} = \begin{bmatrix} v_{a,b}^* \\ v_{b,b}^* \\ v_{c,b}^* \end{bmatrix} = C^{-1} \begin{bmatrix} v_{\alpha,ch}^* \\ v_{\beta,ch}^* \\ 0 \end{bmatrix} \tag{9a}$$

$$\begin{bmatrix} g_{a,t} \\ g_{b,t} \\ g_{c,t} \end{bmatrix} = \begin{bmatrix} g_{a,b} \\ g_{b,b} \\ g_{c,b} \end{bmatrix} = \left(\frac{2}{V_{dc}} \begin{bmatrix} v_{a,t}^* \\ v_{b,t}^* \\ v_{c,t}^* \end{bmatrix} > \begin{bmatrix} c(t) \\ c(t) \\ c(t) \end{bmatrix} \right). \tag{9b}$$

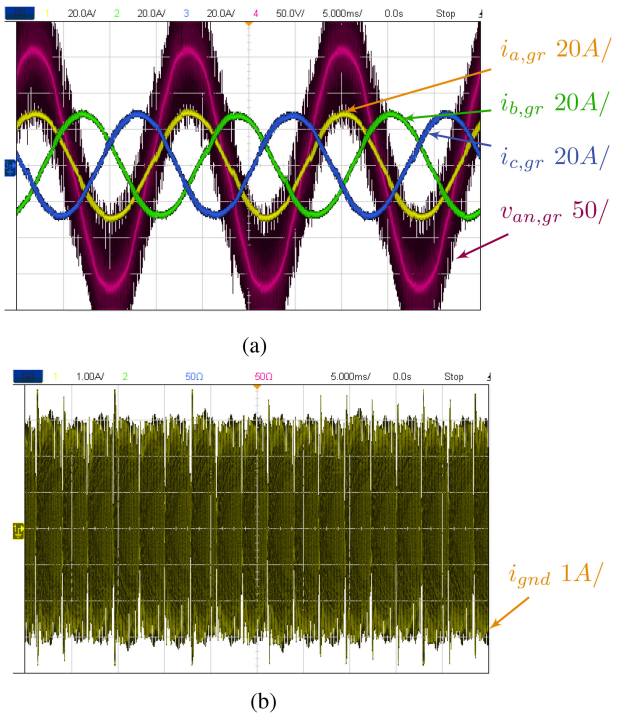

Fig. 13. Experimental results during G2V operation using a conventional PWM. (a) Grid line current and phase voltage. (b) Grid CM current.

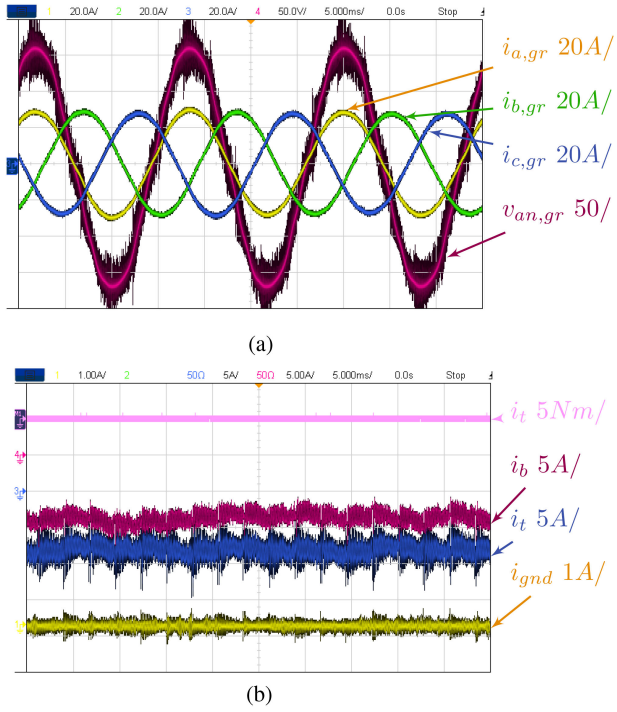

Fig. 14. Experimental results during G2V operation using the proposed modulation. (a) Grid line current and phase voltage. (b) Torque, battery currents, and grid CM current.

G2V operation is conducted once more at 20 A_{rms} and unity power factor. This time the system used the proposed modulation. The results are shown in Fig. 14. Fig. 14(a) shows the measured grid line currents and phase voltage. While the currents are approximately the same, the voltage seems to have less noise. This suggests the noise results from the CM current generated by the conventional modulation scheme. The grid CM current is shown in Fig. 14(b), and measured to be 65.4 mA_{rms}, which represents approximately a 30-fold reduction, despite the underestimation of the CM current in the benchmark case due to sensor saturation.

The torque is also measured and shown in Fig. 14(b) to be approximately zero. The batteries are charged, as evidenced by the negative currents, shown in Fig. 14(b). This result suggests that the modulation meets its CM, torque, and charging objectives.

The test is repeated, this time with V2G operation, at 20 A_{rms} and unity power factor. Fig. 14(a) shows the measured grid line currents and phase voltage. The measured torque, grid CM current, and the battery currents are shown in Fig. 14(b). Once again, no significant torque or CM currents are observed. The only difference to the past test is that the battery currents are positive in the V2G operation, while the grid currents are out of phase with the grid voltage.

The ground-fault current interrupters prescribed by standards do not operate on the exact CM current. Instead, a human body model filter is applied, as prescribed in [27]. The protection trips and the charging stops if the output exceeds 20 MIU. To indicate whether or not the system would trip in the presence of a ground fault current interrupter, the data of the past experiments are exported and filtered using the human body model filter.

TABLE III
SUMMARY OF EXPERIMENTAL CM MEASUREMENTS

Modulation	CM	CM - MIU	Compliant
Conventional	2.0 A_{rms}	308 MIU	×
Proposed	65.4 mA_{rms}	12.6 MIU	✓

The results, along with the original data, are shown in Fig. 16. The unfiltered results are shown in Fig. 16(a). The MIU output of the filter is shown in Fig. 16(b), wherein the conventional modulation has a peak of 308 MIU, while the proposed modulation peaks at 12.6 MIU. The results are summarized in Table III.

The system is operated through a CC–CV cycle to demonstrate the controller performance in a practical setting. Two EA-PSB 10750-120 power supplies units are used. The power supply software is used to emulate the batteries for the experiments. The battery chosen to be emulated for this test is composed of 100 series-connected lithium-ion cells, with 400-V nominal voltage and 20-Ah capacity, characterizing 8 kWh per battery and 16 kWh total storage. This capacity is chosen to limit the time required for the experiment to around 30 min.

In this experiment, the CV controller sets the battery voltage at 410, whereas the CC controller sets the limit of the grid current to 20 A_{rms}, since the machine used in this test has a constant current specification of 20 A_{rms}. As a result, this experiment is conducted at 7.2 kW during the CC operation, gradually decreasing during the CV operation.

The results are shown in Fig. 17. Fig. 17(a) and (b) shows the voltages and currents on the top and bottom batteries, respectively. At the beginning of the test, the system current is set to

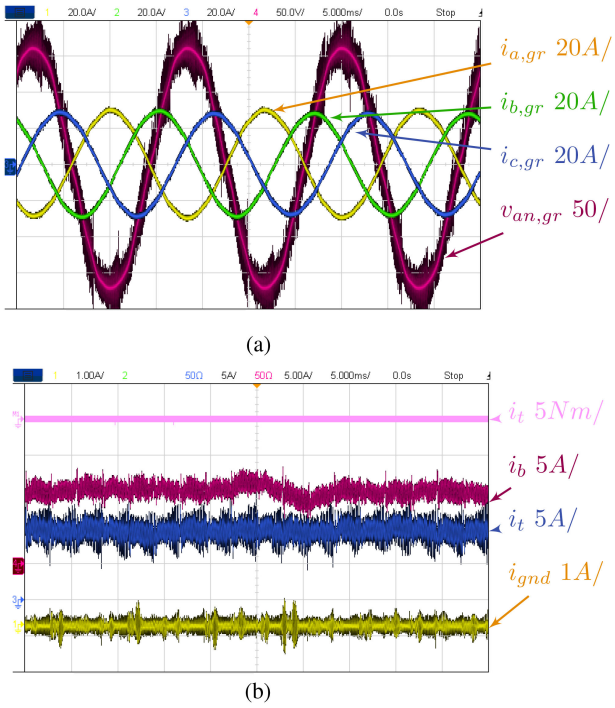

Fig. 15. Experimental results during V2G operation. (a) Grid line current and phase voltage. (b) Torque, battery currents, and grid CM current.

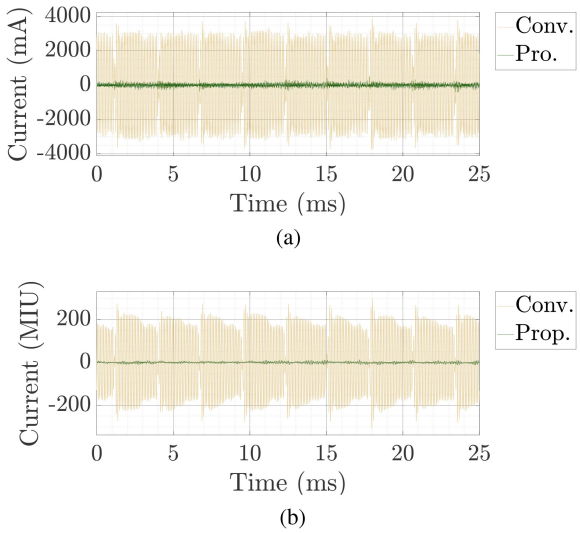

Fig. 16. Experimentally measured CM leakage current reduction by the proposed modulation technique. (a) Ground current. (b) Ground current filtered as prescribed in the standard.

the maximum, causing the battery voltage to rise. After about 15 min of charging, the battery voltage reaches the 410-V set point. At that time, the current setting starts to drop until it reaches 5 A_{rms} at the grid, when the system turns OFF. At that time, the currents are around 2 A through each of the batteries. The SoC reported by the power supply is shown in Fig. 17(c) and (d), detailing the rise from the initial 70% SoC to 89% and the end of the test.

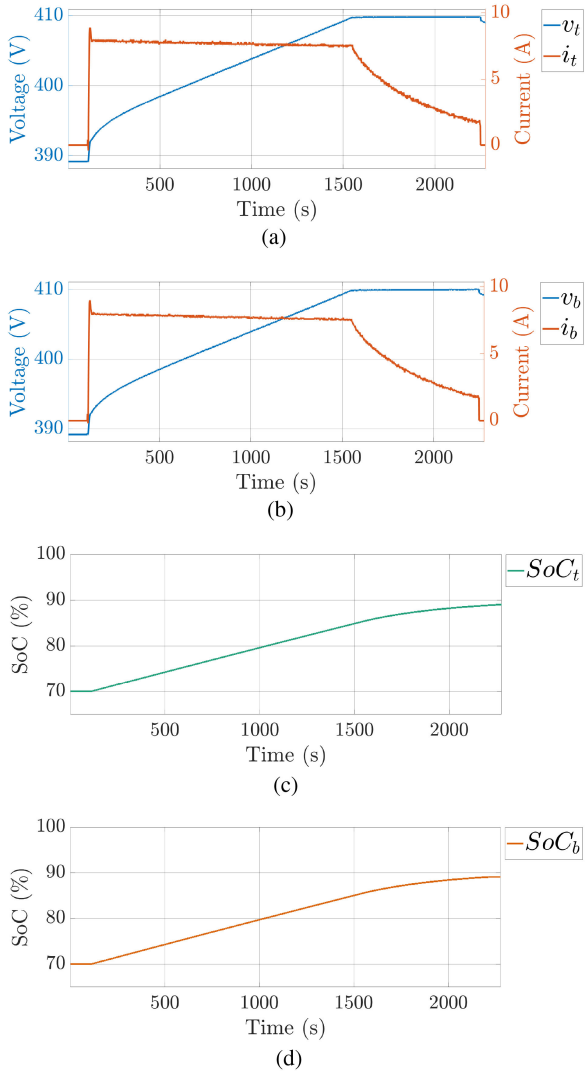

Fig. 17. Experimental results of CC–CV charging operation with battery emulation power supply EA-PSB. Data exported by the battery emulator power supply software. (a) Top battery voltage and currents during charging. (b) Bottom battery voltage and currents during charging. (c) Top battery state of charge during charging. (d) Bottom battery state of charge during charging.

VI. Conclusion

This article presents a topology that can perform nonisolated three-phase charging for EVs using a drivetrain based on the dual-inverter architecture. The model of the system is derived, wherein the circuit is decomposed into four conceptually and mathematically decoupled subsystems, related to 1) charging, 2) driving, 3) CM current, and 4) zero-sequence current generation. By employing a separate dc-link to each inverter, the system prevents circulation of zero-sequence current during driving operation, as demonstrated by the zero-sequence subsystem.

A bespoke SVPWM is proposed using this model, which can be used with the topology introduced here. The introduced modulation ensures vastly superior CM current flowing through the ac grid, compared to a conventional modulation benchmark, in the absence of galvanic isolation, allowing for standard-compliant nonisolated deployment. Simulations and

experimental verification are presented to validate the model, including CC–CV charging of battery emulator power supplies. With the proposed modulation, charging operation is demonstrated to produce zero torque and to reduce the CM currents 30-fold, leading to standard-compliant nonisolated operation.

VI. Appendix

A. Implementation of Proposed Modulation

The general implementation of the modulator introduced in this article can be achieved by the following sequence of steps.

1) Determine the sector i in which the reference voltage $v^*_{\alpha,ch} + jv^*_{\beta,ch}$ lies.
2) Use the switching states sequence

$$\begin{aligned} 18 \rightarrow \quad & (2i)\%12 \quad \rightarrow \ (2i+3)\%12 \rightarrow \\ 19 \rightarrow \ & (2i+1)\%12 \rightarrow \ (2i+2)\%12 \rightarrow \ 18 \end{aligned}$$

   where $(x)\%12$ denotes the reminder of the division of x by 12.
3) Determine the reference voltage rotated to its equivalent voltage in sector s_0

$$\begin{bmatrix} v_{\alpha,s0} \\ v_{\beta,s0} \end{bmatrix} = \begin{bmatrix} \frac{1}{2} & -\frac{\sqrt{3}}{2} \\ \frac{\sqrt{3}}{2} & \frac{1}{2} \end{bmatrix}^i \begin{bmatrix} v^*_{\alpha,ch} \\ v^*_{\beta,ch} \end{bmatrix}. \tag{10}$$

4) Determine the active dwell times, based on

$$\begin{aligned} \begin{bmatrix} t_{(2i)\%12} \\ t_{(2i+2)\%12} \end{bmatrix} &= \begin{bmatrix} t_{(2i+1)\%12} \\ t_{(2i+3)\%12} \end{bmatrix} \\ &= \frac{\sqrt{3}}{2V_{dc}f_{sw}} \begin{bmatrix} 0 & \frac{\sqrt{3}}{2} \\ -1 & -\frac{1}{2} \end{bmatrix}^{-1} \begin{bmatrix} v^*_{\alpha,s0} \\ v^*_{\beta,s0} \end{bmatrix}. \end{aligned} \tag{11}$$

5) Determine the zero-vector dwell times, based on

$$t_{18} = t_{19} = \frac{1}{2f_{sw}} - \left(t_{(2i)\%12} + t_{(2i+2)\%12}\right). \tag{12}$$

References

[1] M. Longo, D. Zaninelli, F. Viola, P. Romano, and R. Miceli, "How is the spread of the electric vehicles?," in *Proc. IEEE 1st Int. Forum Res. Technol. Soc. Ind.*, 2015, pp. 439–445.

[2] Y. Xiao and M. Van Der Schaar, "Optimal intervention for incentivizing the adoption of commercial electric vehicles," in *Proc. IEEE Glob. Conf. Signal Inf. Process.*, 2016, pp. 508–512.

[3] D. Pevec, J. Babic, A. Carvalho, Y. Ghiassi-Farrokhfal, W. Ketter, and V. Podobnik, "Electric vehicle range anxiety: An obstacle for the personal transportation (r)evolution?," in *Proc. 4th Int. Conf. Smart Sustain. Technol.*, 2019, pp. 1–8.

[4] M. Yilmaz and P. T. Krein, "Review of integrated charging methods for plug-in electric and hybrid vehicles," in *Proc. IEEE Int. Conf. Veh. Electron. Saf.*, 2012, pp. 346–351.

[5] H. Tu, H. Feng, S. Srdic, and S. Lukic, "Extreme fast charging of electric vehicles: A technology overview," *IEEE Trans. Transport. Electrific.*, vol. 5, no. 4, pp. 861–878, Dec. 2019.

[6] M. Y. Metwly, M. S. Abdel-Majeed, A. S. Abdel-Khalik, R. A. Hamdy, M. S. Hamad, and S. Ahmed, "A review of integrated on-board EV battery chargers: Advanced topologies, recent developments and optimal selection of FSCW slot/pole combination," *IEEE Access*, vol. 8, pp. 85216–85242, 2020.

[7] I. Subotic, N. Bodo, E. Levi, and M. Jones, "Onboard integrated battery charger for EVs using an asymmetrical nine-phase machine," *IEEE Trans. Ind. Electron.*, vol. 62, no. 5, pp. 3285–3295, May 2015.

[8] H. J. Raherimihaja, Q. Zhang, G. Xu, and X. Zhang, "Integration of battery charging process for EVs into segmented three-phase motor drive with V2G mode capability," *IEEE Trans. Ind. Electron.*, vol. 68, no. 4, pp. 2834–2844, Apr. 2021.

[9] S. Loudot, B. Briane, O. Ploix, and A. Villeneuve, "Fast charging device for an electric vehicle," U.S. Patent 2012/028674.0 A1, 2012.

[10] P. Gray, P. Lehn, and S. Wang, "An integrated bidirectional three-phase AC charger for vehicle applications with buck-boost capability," in *Proc. IEEE Energy Convers. Congr. Expo.*, 2018, pp. 517–523.

[11] S. Wang and P. W. Lehn, "Design and control of 3-phase integrated charger for dual-inverter drivetrain electric vehicles," in *Proc. IEEE Transp. Electrific. Conf. Expo*, 2019, pp. 1–6.

[12] C. Shi, Y. Tang, and A. Khaligh, "A three-phase integrated onboard charger for plug-in electric vehicles," *IEEE Trans. Power Electron.*, vol. 33, no. 6, pp. 4716–4725, Jun. 2018.

[13] R. Shi, S. Semsar, and P. W. Lehn, "Constant current fast charging of electric vehicles via a DC grid using a dual-inverter drive," *IEEE Trans. Ind. Electron.*, vol. 64, no. 9, pp. 6940–6949, Sep. 2017.

[14] S. Semsar, T. Soong, and P. W. Lehn, "Integrated single-phase electric vehicle charging using a dual-inverter drive," in *Proc. IEEE Transp. Electrific. Conf. Expo*, 2018, pp. 320–325.

[15] S. Semsar, T. Soong, and P. W. Lehn, "On-board single-phase integrated electric vehicle charger with V2G functionality," *IEEE Trans. Power Electron.*, vol. 35, no. 11, pp. 12072–12084, Nov. 2020.

[16] L. De Sousa, B. Silvestre, and B. Bouchez, "A combined multiphase electric drive and fast battery charger for electric vehicles: Topology and electric propulsion efficiency analysis," in *Proc. IEEE Veh. Power Propulsion Conf.*, 2010, pp. 1–6.

[17] A. Bruyère, L. De Sousa, B. Bouchez, P. Sandulescu, X. Kestelyn, and E. Semail, "A multiphase traction/fast-battery-charger drive for electric or plug-in hybrid vehicles: Solutions for control in traction mode," in *Proc. IEEE Veh. Power Propulsion Conf.*, 2010, pp. 1–7.

[18] W. Lhomme, P. Delarue, X. Kestelyn, P. Sandulescu, and A. Bruyere, "Control of a combined multiphase electric drive and battery charger for electric vehicle," in *Proc. 15th Eur. Conf. Power Electron. Appl.*, 2013, pp. 1–10.

[19] W. Lhomme et al., "Integrated traction/charge/air compression supply using three-phase split-windings motor for electric vehicles," *IEEE Trans. Power Electron.*, vol. 33, no. 11, pp. 10003–10012, Nov. 2018.

[20] S. Lacroix, E. Laboure, and M. Hilairet, "An integrated fast battery charger for electric vehicle," in *Proc. IEEE Veh. Power Propulsion Conf.*, 2010, pp. 1–6.

[21] I. Subotic, N. Bodo, and E. Levi, "Integration of six-phase EV drivetrains into battery charging process with direct grid connection," *IEEE Trans. Energy Convers.*, vol. 32, no. 3, pp. 1012–1022, Sep. 2017.

[22] S. Q. Ali, D. Mascarella, G. Joos, and L. Tan, "Torque cancelation of integrated battery charger based on six-phase permanent magnet synchronous motor drives for electric vehicles," *IEEE Trans. Transport. Electrific.*, vol. 4, no. 2, pp. 344–354, Jun. 2018.

[23] S. Q. Ali, D. Mascarella, G. Joos, and L. Tan, "Torque elimination for integrated battery charger based on two permanent magnet synchronous motor drives for electric vehicles," *IET Electric Power Appl.*, vol. 11, no. 9, pp. 1627–1635, 2017.

[24] V. Vidya and R. S. Kaarthik, "A control scheme for integrated battery charger with split-phase machine," in *Proc. IEEE Int. Conf. Power Electron., Smart Grid, Renewable Energy*, 2020, pp. 1–6.

[25] V. V. and R. S. Kaarthik, "Modeling and control of an integrated battery charger with split-phase machine," *IEEE Trans. Ind. Appl.*, vol. 57, no. 2, pp. 1588–1597, Mar./Apr. 2021.

[26] *Electric Vehicle Conductive Charging System - Part 23: DC Electric Vehicle Charging Station*, International Electrotechnical Commission, Standard IEC 61851–23:2014, 2014. [Online]. Available: http://webstore.iec.ch/publication/6032

[27] *Standard for Safety for Personnel Protection Systems for Electric Vehicle (EV) Supply Circuits: General Requirements*, Underwriting Laboratories, Standard IEC 2231-1:2016, 2016. [Online]. Available: https://standardscatalog.ul.com/ProductDetail.aspx?UniqueKey=24886

[28] H. Xiao, "Overview of transformerless photovoltaic grid-connected inverters," *IEEE Trans. Power Electron.*, vol. 36, no. 1, pp. 533–548, Jan. 2021.

[29] A. A. Estévez-Bén, A. Alvarez-Diazcomas, G. Macias-Bobadilla, and J. Rodríguez-Reséndiz, "Leakage current reduction in single-phase grid-connected inverters — A review," *Appl. Sci.*, vol. 10, no. 7, pp. 1–26, 2020.

[30] K. Zeb et al., "An overview of transformerless inverters for grid connected photovoltaic system," in *Proc. Int. Conf. Comput., Electron., Elect. Eng.*, 2019, pp. 1–6.
[31] C. Viana, N. Yakop, D. Frost, and P. Lehn, "A symmetrical boost converter with reduced common-mode leakage currents for EV applications," in *Proc. 22nd Eur. Conf. Power Electron. Appl.*, 2020, pp. 1–8.
[32] C. Viana, S. Semsar, M. Pathmanathan, and P. W. Lehn, "Generalized method for designing nonisolated safety standard compliant onboard chargers for electric vehicles," in *Proc. IECON Proc. (Ind. Electron. Conf.)*, 2021, pp. 1–6.
[33] C. Viana, S. Semsar, M. Pathmanathan, and P. W. Lehn, "Integrated transformerless EV charger with symmetrical modulation," *IEEE Trans. Ind. Electron.*, to be published, doi: 10.1109/TIE.2021.3127032.
[34] Y. Zhang et al., "Leakage current mitigation of non-isolated integrated chargers for electric vehicles," in *Proc. IEEE Energy Convers. Congr. Expo.*, 2019 pp. 1195–1201.
[35] Y. Zhang et al., "Leakage current issue of non-isolated integrated chargers for electric vehicles," in *Proc. IEEE Energy Convers. Congr. Expo.*, 2018, pp. 1221–1227.
[36] Y. Lee and J.-I. Ha, "Hybrid modulation of dual inverter for open-end permanent magnet synchronous motor," *IEEE Trans. Power Electron.*, vol. 30, no. 6, pp. 3286–3299, Jun. 2015.
[37] S. Singh, C. Perera, G. J. Kish, and J. Salmon, "PWM control of a dual inverter drive using a floating capacitor inverter," in *Proc. IEEE 20th Workshop Control Model. Power Electron.*, 2019, 1–8.
[38] S. Singh, C. Perera, G. J. Kish, and J. Salmon, "Low harmonic loss PWM for a dual inverter drive using a floating capacitor inverter," in *Proc. IEEE Energy Convers. Congr. Expo.*, 2019, pp. 5981–5988.
[39] R. Menon, S. S. Williamson, N. A. Azeez, and A. H. Kadam, "A fault tolerant modulation strategy for dual inverter traction drives," in *Proc. IEEE Energy Convers. Congr. Expo.*, 2019, pp. 5856–5861.
[40] M. Pathmanathan, C. Viana, S. Semsar, and P. Lehn, "Open-phase fault tolerant driving operation of dual-inverter-based traction drive," *IET Electric Power Appl.*, vol. 15, no. 7, pp. 873–889, 2021.
[41] M. Pathmanathan, S. Semsar, C. Viana, and P. W. Lehn, "Power sharing control algorithm for direct integration of fuel cells in a dual-inverter electric vehicle drivetrain," *IEEE Trans. Transport. Electrific.*, vol. 8, no. 2, pp. 2490–2500, Jun. 2022.
[42] R. Shi, S. Semsar, and P. W. Lehn, "Coordinated power sharing for enhanced utilization of mixed energy storage media in dual-inverter electric vehicles," in *Proc. IEEE Int. Electric Mach. Drives Conf.*, 2019, pp. 1586–1592.
[43] A. R. Chandran, M. D. Hennen, A. Arkkio, and A. Belahcen, "Safe turn-off strategy for electric drives in automotive applications," *IEEE Trans. Transport. Electrific.*, vol. 8, no. 1, pp. 9–22, Mar. 2022.
[44] B. Welchko, T. Jahns, W. Soong, and J. Nagashima, "IPM synchronous machine drive response to symmetrical and asymmetrical short circuit faults," *IEEE Trans. Energy Convers.*, vol. 18, no. 2, pp. 291–298, Jun. 2003.

Caniggia Viana (Student Member, IEEE) received the B.A.Sc. degree in electrical engineering from the Federal University of Rio Grande do Norte, Natal, Brazil, in 2017. He is currently working toward the Ph.D. degree in electrical engineering with the University of Toronto, Toronto, ON, Canada.

His research interests include electric vehicle drivetrains, integrated chargers for electric vehicles, and standard compliant transformerless conversion.

Mehanathan Pathmanathan (Senior Member, IEEE) received the B.E. (Hons.) and Ph.D. degrees in electrical and electronic engineering from The University of Adelaide, Adelaide, SA, Australia, in 2007 and 2012, respectively.

From 2012 to 2018, he was a Research Engineer with Machines and Drives Team, ABB Corporate Research, Sweden. Since 2018, he has been a Research Associate with the University of Toronto, Toronto, ON, Canada. His research interests include electric vehicle powertrains, medium-voltage drives, and wireless power transfer.

Peter W. Lehn (Senior Member, IEEE) received the B.Sc. and M.Sc. degrees in electrical engineering from the University of Manitoba, Winnipeg, MN, Canada, in 1990 and 1992, respectively, and the Ph.D. degree in electrical and computer engineering from the University of Toronto, Toronto, ON, Canada, in 1999.

He was the Faculty with the University of Toronto, in 1999. He was a Visiting Professor with the University of Erlangen-Nuremberg, in 2001. His research interests include HVdc technologies, grid integration of storage and renewables, power electronics for electric vehicles, and theoretical analysis of power electronic systems.

Dr. Lehn was an Editor of the IEEE TRANSACTIONS ON ENERGY CONVERSION from 2013 to 2019.